Research Article

Journal of the Optical Society of America B

OPTICAL PHYSICS

Decoherence due to XPM-assisted Raman amplification for polarization or wavelength offset pulses in all-normal dispersion supercontinuum generation

JAMES S. FEEHAN[1,*] AND JONATHAN H. V. PRICE[2]

[1]Scottish Universities Physics Alliance, Department of Physics, University of Strathclyde, Glasgow G4 0NG, UK
[2]Optoelectronics Research Centre, University of Southampton, Hampshire, SO17 1BJ, UK
*Corresponding author: james.feehan@strath.ac.uk

Received 2 October 2019; revised 5 December 2019; accepted 9 December 2019; posted 11 December 2019 (Doc. ID 379563); published 11 February 2020

We report the importance of cross-phase modulation (XPM) on the coherence of a low-energy probe pulse co-propagating with a high-energy pump pulse that generates incoherent supercontinuum in all-normal dispersion (ANDi) fiber due to Raman amplification of quantum noise. By investigating numerous fiber and pulse parameters, we show consistently that for weak probe pulses, the XPM from the pump is the dominant influence on the degradation of the probe coherence. We show that the faster decoherence at the pump leading edge means that the probe coherence is reduced more significantly when the probe has a higher group velocity, i.e., when an orthogonally polarized probe is aligned to the fast (lower refractive index) axis of the fiber or when a co-polarized probe has a longer central wavelength. Simulations show that this effect occurs for both polarization-maintaining (PM) and non-PM ANDi fibers and can result in a probe decoherence rate that is higher than that of the pump. These previously unreported results extend our earlier scalar simulations showing incoherent supercontinuum within a single pulse.

https://doi.org/10.1364/JOSAB.379563

1. INTRODUCTION

Supercontinuum generation in all-normal dispersion (ANDi) specialty and photonic crystal fibers (PCFs) [1–3] has gathered significant interest due to ANDi fibers having a unique combination of both tight mode confinement and a low, flat, and single-signed dispersion profile. This permits a monotonic positive chirp across the entire final supercontinuum spectrum following its initial generation through the optical wavebreaking process [4,5]. ANDi fibers therefore provide access to broadband, dissipative nonlinear propagation solutions that maintain several desirable features of the input driving pulses, such as a single-peaked time-domain distribution and smoothly varying phase [6,7]. Such fibers have become a popular platform for generating high-brightness pulses that are compressible to the single-cycle limit [8].

Recent numerical and experimental investigations have revealed that an almost perfect output spectral coherence can be achieved using pump pulses with durations up to 1.5 ps [9], ensuring excellent shot-to-shot amplitude and phase stability. This broadens the types of seed lasers that can be used when compared with pumping in the anomalous dispersion regime, which typically requires pulses shorter than ~ 150 fs to mitigate the influence of quantum noise [10]. The complexity and cost of coherent supercontinuum sources can therefore be reduced when using ANDi fiber. Applications include optical coherence tomography [11,12], as well as spectroscopy and frequency metrology [13,14] with possible extension to gigahertz repetition rates [15]. Additionally, with the recent development of ANDi fibers with dispersion minima and low loss at wavelengths around $1.5-2$ μm [16–18], the possibilities now extend to the mid-infrared [17,19], opening new opportunities for research in molecular fingerprinting [20] and silicon photonics [21].

For pulse durations above ~ 1.5 ps, Raman gain coupled with the characteristic steep-edged, flat-top spectra in the ANDi regime [3,7] leads to the amplification of out-of-band quantum noise [9]. This is distinct from coherent energy transfer between pulse-seeded spectral components, which is the desired process in both the ANDi regime and in soliton self-frequency

shifting in the anomalous dispersion regime [10,22,23]. Noise amplification is accelerated by the parametric amplification of higher-order Stokes and anti-Stokes waves through four-wave mixing (FWM) under non-phase-matched conditions [24–26] when the coherent self phase modulation (SPM) and optical wavebreaking processes fail to dominate the pulse propagation, and when the competing Raman-assisted parametric FWM process is not effectively suppressed [9]. Hence, the competition between optical wavebreaking and Raman-assisted parametric FWM is of central importance to the rate of decoherence of multi-picosecond pulses in ANDi fibers [9,27]. Developing a more complete understanding of the processes that limit coherent spectral broadening in the ANDi regime has therefore remained at the forefront of recent research [9,28,29].

Nonlinear coupling between optical signals through cross-phase modulation (XPM) is a commonly used technique with applications in all-optical switching [30], multiplexing [31], and modelocking [32,33]. However, its influence on nonlinear dynamics in ANDi fiber has remained largely unexplored. Recent contributions have focused on the role of XPM in vector modulation instability (MI) [28], building on previous studies that introduced this effect using normal-dispersion pumping in step-index silica fibers [34,35].

Here, we investigate vector propagation effects in ANDi PCFs and show how they can couple with the Raman amplification of out-of-band quantum noise and pulse decoherence. Vector contributions to Raman-based decoherence have not previously been studied. We investigate the output coherence of a low-energy probe pulse that propagates with a high-energy, incoherent supercontinuum-generating pulse as a function of temporal walkoff due to differing wavelengths or polarization state, thereby generalizing previous scalar reports [9]. We focus on a central wavelength of 1040 nm, pulse energies around 60 nJ, and peak powers up to 15 kW. These pulse parameters approximate those output by commonly used sources such as femto- and picosecond Yb-fiber lasers operating at megahertz repetition rates. Additionally, non-polarization-maintaining (PM) and PM fibers are considered by adjusting the group velocity mismatch (GVM) between the pump and probe over the range of 0 to ±10 ps/m [36,37].

While in experiments the choice of seed laser will cause specific parameters such as peak power thresholds and fiber lengths to vary from those presented in this work, the main conclusions will apply to seeding with titanium sapphire lasers as well as Yb-fiber lasers, and to mid-infrared sources used with chalcogenide ANDi fiber [17]. The findings may also be applicable to picosecond and femtosecond fiber amplifier and oscillator design, especially where optical wavebreaking is suppressed and the critical power for Raman amplification is exceeded [38].

The model is detailed in Section 2 with supplementary material in Appendix A. In Section 3, we show how XPM and Raman amplification couple to cause decoherence between co-propagating pulses. Orthogonally polarized pulses are considered in Section 3.A. We investigate the probe coherence as the pump transitions from coherent to incoherent dynamics (Section 3.A.1) and show that the probe decoherence can occur faster than the pump (Section 3.A.2). Co-polarized pulses with different central wavelengths are then studied in Section 3.B. Section 4 concludes the paper.

2. NUMERICAL METHODS

To model the influence of XPM on the coherence, we used the pump–probe approach outlined in Fig. 1. We consider transform-limited Gaussian input pulses for both the pump and probe, with a temporal field envelope given by $A(T) = \sqrt{P_0}\exp[-2\ln(2)(T/T_0)^2]$. ($T$ is the retarded time in the co-moving frame of reference traveling at the group velocity of the pump pulse central wavelength, and T_0 is the full width at half maximum pulse duration and is equal for the pump and probe unless otherwise specified.) Peak powers were on the order of kiloWatts and Watts for the pump and probe, respectively, so they experienced different degrees of spectral broadening as demonstrated by the example of orthogonally polarized pump and probe in a birefringent PCF shown in the right-hand plot of Fig. 1.

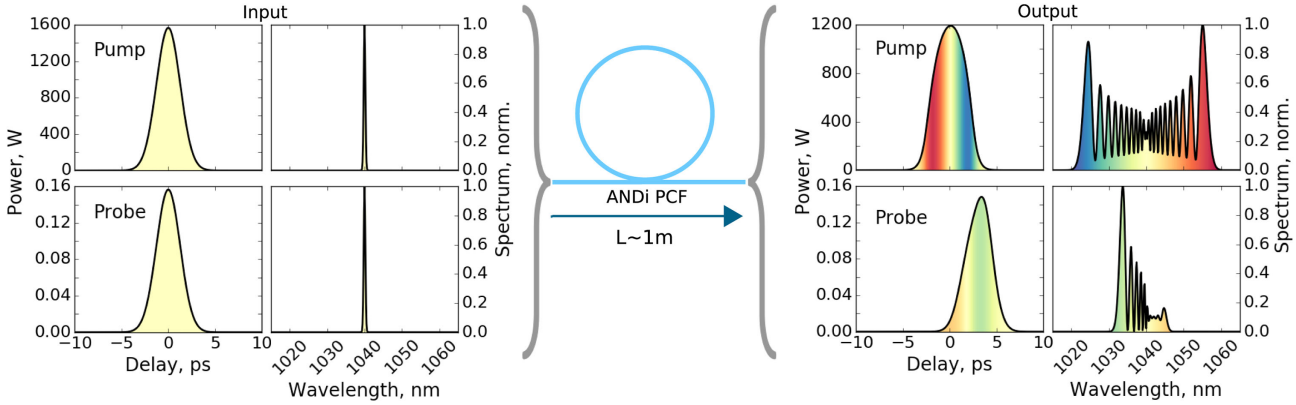

Fig. 1. Left (input pulses): the propagation of transform-limited high-energy pump (top row) and low-energy probe (bottom row) pulses in ANDi PCF is simulated to investigate how the pump modifies the probe coherence. This is done by tuning the GVM between the pump and probe, accessed using the fiber birefringence and probe central wavelength. Right (output pulses): the colormaps under the time-and frequency-domain plots have been matched to indicate how the pump and probe spectra are distributed in the time domain. The asymmetric spectral broadening of the probe shows that XPM driven by the pump pulse dominates, and that SPM within the probe is negligible. Equation (1) is therefore satisfied.

Our choice of pulse parameters was determined by the inequalities shown by Eqs. (1) and (2). These ensured that any nonlinear propagation effects and resulting decoherence experienced by the probe were driven entirely by the pump, and that the fiber length was sufficient for the pump to undergo incoherent spectral broadening. In Eq. (1), $L_N = 1/(\gamma P_0)$ is the nonlinear length, $\gamma = kn_2/A_{\text{eff}}$ parameterizes the fiber nonlinear response, and P_0 is the pulse peak power:

$$L_{N\,\text{probe}} \gg L_{\text{fiber}} \gg L_{N\,\text{pump}}, \tag{1}$$

$$L_{WB} > L_R^{\star}. \tag{2}$$

Here, $L_{WB} \approx 1.1\sqrt{L_N L_D}$ is the wavebreaking length [6], and $L_D = T_0^2/|\beta_2|$ is the dispersion length. The Raman length is defined as $L_R^{\star} = 1/(g_s^{\star} P_0)$ [9], where $g_s^{\star}$ is the mixed parametric-Raman peak gain coefficient [24–26], given by Eq. (3):

$$g_s^{\star} = 2\gamma\,\text{Re}\left(\sqrt{K(2q-K)}\right). \tag{3}$$

$K = -\beta_2\Omega_R^2/(2\gamma P_0)$ is the linear phase mismatch between the seed pulse and (anti)-Stokes wave normalized to the nonlinear contribution to the mismatch, $q = (1 - f_R) + f_R\tilde{\chi}_R^{(3)}(-\Omega_R)$, and $\tilde{\chi}_R^{(3)}(-\Omega_R)$ is the complex Raman susceptibility [9]. The Raman effect was included using the experimentally measured silica response [39] via a fractional contribution to the nonlinear response of $f_R = 0.18$ and a maximum $\tilde{\chi}_R^{(3)} = -1.38i$ at a frequency detuning of $\Omega_R/(2\pi) = 13.2$ THz.

The vector generalized nonlinear Schrödinger equation (GNLSE) included polarization dynamics and interactions between pulses resulting from XPM, and is detailed in appendix A. The GNLSE was integrated using the Runge–Kutta fourth-order interaction picture method (RK4IP) [40] along with the conservation quantity error method (CQEM, [41]) adaptive step sizing technique for a negligible integration error [42]. The CQEM ensured that the total photon number over both the pump and probe pulses was conserved (accounting for loss) so that energy transfer between the pump and probe was permitted.

We considered a hexagonal-lattice silica ANDi PCF with pitch and relative hole size of $\Lambda = 1.7$ μm and $d/\Lambda = 0.3$, giving $\max(D(\lambda)) = -31$ ps/(nm km) and $\gamma = 0.027$ rad(Wm)$^{-1}$ at 1040 nm. (The wavelength dependence of γ was also included.) The dispersion profile (Fig. 2) was calculated using an analytical approach [43,44]. Fiber loss was included using a measured loss spectrum for standard single-mode silica fibers digitized from Ref. [45] (Fig. 2). To simplify the calculations, $D(\lambda)$ and A_{eff} (and hence γ) were the same for both birefringence axes. For orthogonally polarized pump and probe pulses, the polarization-dependent GVM was included using $\Delta\beta_1 = \beta_{1\,\text{pump}} - \beta_{1\text{probe}}$, where β_1 is the inverse group velocity. The GVM for co-polarized pump and probe pulses was determined by the fiber dispersion. The XPM contribution was also modified depending on the relative polarization by modifying XPM relative to SPM by $\epsilon_{\text{XPM}} = 2/3$ or 2 for orthogonal and parallel polarization states, respectively [46] [Appendix A, Eq. (A3)]. This method of incorporating XPM and the polarization GVM has been used to accurately model vector nonlinear propagation [47]. Spontaneous Raman scattering noise was also included [10,48].

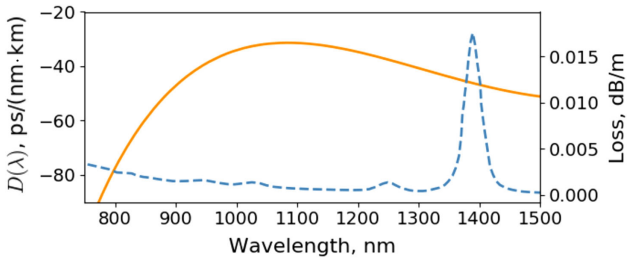

Fig. 2. Left axis (orange solid): dispersion curve for the silica hexagonal-lattice ANDi PCF. $\Lambda = 1.7$ μm, and $d/\Lambda = 0.3$. Right axis (blue dashed): loss profile used in the simulations.

Shot noise was included in the simulations using the standard one photon per mode approach [10]. Although noise levels above the quantum limit cause a more rapid reduction in coherence [9] and have been shown to influence the propagation dynamics [29,49], our focus was to explore the combined effect of XPM and Raman amplification, so we assume quantum noise limited seed lasers. We consider pulse durations between 100 fs and 7 ps, implying the use of mode-locked lasers, which have excellent noise properties [50]. Pulse peak powers were restricted to < 100 kW so we did not expect to see incoherent optical wavebreaking or incoherent cloud formation [9] over the meter-length fibers used. The generality of our work is therefore not reduced by considering only quantum noise limited seed pulses for the pulse energies and peak powers investigated.

The shot-to-shot output spectral stability was calculated over an ensemble of independently generated pairs of spectra using the modulus of the first-order degree of coherence and its average (denoted by angular brackets), defined by Eqs. (4) and (5), respectively [51,52]. These equations were applied to the pump and probe ensembles separately:

$$\left|g_{12}^{(1)}(\lambda, t_a - t_b)\right| = \left|\frac{\langle A_a^{\star}(\lambda, t_a) A_b(\lambda, t_b)\rangle}{\sqrt{\langle|A_a(\lambda, t_a)|^2\rangle\langle|A_b(\lambda, t_b)|^2\rangle}}\right|_{a\neq b}, \tag{4}$$

$$\langle|g_{12}^{(1)}|\rangle = \frac{\int_0^{\infty}|g_{12}^{(1)}||A(\lambda)|^2 d\lambda}{\int_0^{\infty}|A(\lambda)|^2 d\lambda}. \tag{5}$$

Each simulation comprised 24 individual shots (276 pairs of spectra, sufficient for the averaging [9,10]). Equations (4) and (5) are defined over the interval [0; 1], with a value of 1 indicating perfect coherence.

The fiber length over which $\langle|g_{12}^{(1)}|\rangle$ decreases to 0.9 is the coherence length, L_c. Its dependence on the pulse duration is expressed in Eq. (6), and while an approximate analytic formula exists [9], we circumvent the need for numerical fitting by calculating $\langle|g_{12}^{(1)}|\rangle$ directly as a function of fiber length during the simulations:

$$L_c \propto \frac{1}{f_R\Omega_R T_0}. \tag{6}$$

Alternatively, the coherence length can also be expressed as $L_c \propto L_R^{\star}/L_{WB}$ [9] [see Eq. (3) for the definition of L_{WB} and $L_R^{\star}$].

Although the ANDi regime does not permit solitons, the soliton number [Eq. (7)] is a useful parameter for interpreting the results:

$$N=\sqrt{\frac{L_{\mathrm{D}}}{L_{\mathrm{N}}}}. \tag{7}$$

3. DECOHERENCE DUE TO XPM-ASSISTED RAMAN AMPLIFICATION

We first explore how the coherence of an orthogonally polarized probe is affected by XPM-assisted Raman amplification (Section 3.A) and then show the effect of the competition between the coherent optical wavebreaking process with Raman-assisted parametric FWM in the pump (Section 3.A.1). We then show how the probe energy affects the probe coherence (Section 3.A.2). The second mode of decoherence with co-polarized but offset wavelength pulses is studied in Section 3.B. The XPM-assisted decoherence process generally follows a four-step pattern:

1. The pump pulse undergoes a combination of FWM and Raman scattering, amplifying Stokes and anti-Stokes waves that are seeded by quantum noise and therefore have stochastic amplitude and phase profiles. This essentially scalar process degrades the pump coherence following the pattern identified in Ref. [9].
2. The pump Stokes and anti-Stokes waves interfere with the main part of the pump to produce stochastic time-domain intensity modulations that are amplified with propagation distance.
3. While the pump and probe overlap in the time domain, XPM transfers the stochastic Raman-amplified intensity modulations of the pump pulse to a stochastic phase modulation in the probe.
4. This phase modulation drives Raman-assisted parametric FWM in the probe, which develops noise-seeded, incoherent Stokes and anti-Stokes spectral sidebands, degrading the probe coherence.

A. Cross-Polarization Decoherence

Figure 3 shows the pump and probe at the output of a 1.3 m length of the ANDi PCF (representative of lengths used in recent studies of supercontinuum decoherence in ANDi fiber [9,27–29]). Here, $E_{\mathrm{pump}}=60$ nJ ($N_{\mathrm{pump}}=770$), $E_{\mathrm{probe}}=5$ pJ, and $\Delta\beta_1=0$ ps/m. The pump has undergone significant spectral broadening as described in step 1 above and in scalar reports of Raman-induced decoherence in ANDi fiber. Strong Stokes and anti-Stokes bands are visible in the ensemble average as a shallow spectral modulation with a frequency corresponding to the Raman gain peak at 13.2 THz. The time-domain modulations outlined in step 2 are visible on the left-hand side, and the coherence of the spectral components resulting from the noise-seeded broadening is low.

The probe ensemble (second row) shows spectral broadening through XPM-assisted Raman amplification outlined in steps 3 and 4, which results in very low probe coherence. It is not possible to characterize this effect using a scalar model alone:

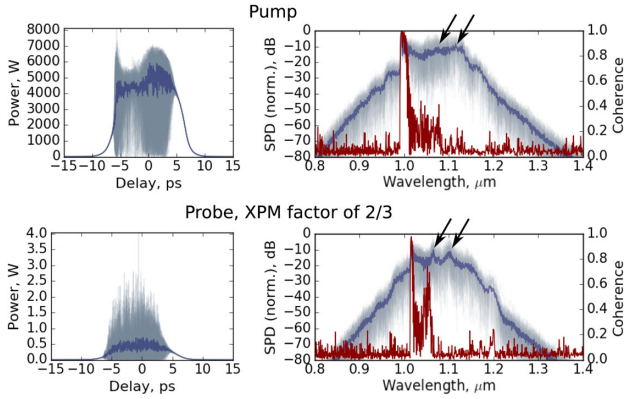

Fig. 3. Orthogonally polarized pump and probe ensembles after co-propagating in silica ANDi PCF with $\Delta\beta_1=0$ ps/m. Left column: time-domain. Right column: normalized spectral power density (SPD, left y axis) and coherence data (red trace, right y axis). Blue traces show the ensemble average, and fine gray lines show the individual shots. Top: pump (60 nJ, 7 ps). Bottom: probe (5 pJ, 7 ps). The arrows mark the two most energetic Stokes peaks.

the output probe ensemble without the XPM term was always coherent. XPM dominates the probe propagation, as the spectral broadening is driven externally (as opposed to SPM in the pump propagation), leading the initially identical pump and probe spectra to evolve differently. The one feature common to the pump and probe is a pair of Raman peaks (first and second Stokes, highlighted by the black arrows), with a spacing equal to the frequency of the main peak in the Raman response of silica (13.2 THz). However, these features also differ in detail, with those in the probe spectrum having narrower bandwidths and shorter central wavelengths.

The origin of these differing characteristics is illustrated in Fig. 4 for 90 cm of PCF and $\Delta\beta_1=7$ ps/m, so that the probe advances through the pump, but neither the pump nor probe becomes fully incoherent, so it is easier to distinguish each nonlinear process. XPM-assisted Raman amplification in the probe is seen directly: the Stokes and anti-Stokes waves in both pulses occur at the same delay (−4 ps). The weaker contribution of XPM to the probe versus SPM to the pump means that the chirp at −4 ps is lower for the probe. Coupled with the common Raman modulation frequency of $\Omega_{\mathrm{R}}/(2\pi)=13.2$ THz, this leads to the probe Raman bands having different central frequencies to the pump Raman bands. The Raman bands of the probe also have narrower bandwidths because the probe has undergone less broadening than the pump, and so the Raman bands are generated from a narrower initial spectrum. The XPM-assisted Raman amplification is purely a phase effect, evidenced by the chirp of each pump/probe Raman band, which closely matches that of the pump/probe pulses, showing that the probe Raman amplification occurs without transferring photons across polarization axes [46]. This is also confirmed by the pump and probe energies, which remain stable apart from loss.

The continuous Raman amplification seen in Fig. 4 would be truncated if, instead of being positive, $\Delta\beta_1$ becomes negative so as to minimize the temporal overlap of the probe with the pump Raman band at its leading edge. An asymmetry in probe

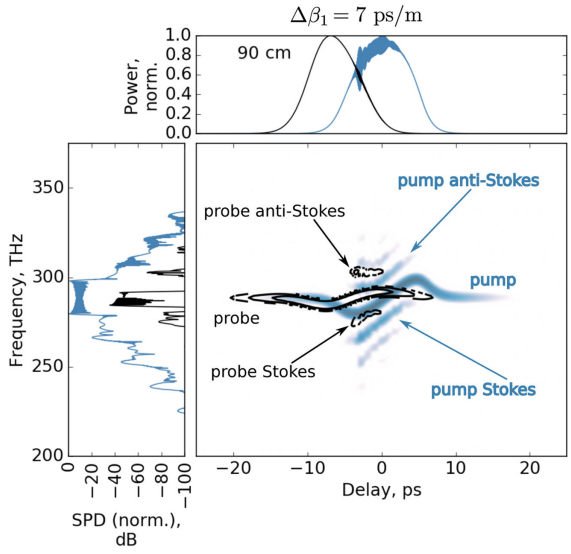

Fig. 4. Spectrograms of orthogonally polarized pump (blue colormap) and probe (black contour) with the same initial central wavelength (1040 nm, 288 THz) after propagating through 90 cm of ANDi PCF with $\Delta\beta_1 = 7$ ps/m. The spectrograms are normalized to the peak of the pump pulse (−70 to 0 dB).

decoherence versus the sign of the GVM is a clear effect of incorporating XPM. To illustrate this, the incoherent broadening of the probe by the pump for $\Delta\beta_1$ values of 7, −7, and 10 ps/m is shown from left to right in Fig. 5 for a 130 cm length of the PCF (all other parameters are the same as those in Figs. 3 and 4). In all cases, the pump Raman scattering was mainly confined to the pump leading edge, as the temporal walkoff between the pump Stokes and anti-Stokes waves was negligible due to the low fiber dispersion of −31 ps/(nm km).

The left-hand plot of Fig. 5 ($\Delta\beta_1 = 7$ ps/m) is the same as Fig. 4 but for 130 cm of PCF instead of 90 cm. The longer interaction length and large temporal overlap has allowed the pump to continuously stimulate Raman amplification in the probe, causing its average coherence to degrade to $\langle|g_{12}^{(1)}|\rangle = 0.15$. Energy transfer from the probe to its incoherent Stokes waves was significant (highlighted in the figure by the red dashed lines).

This changes for $\Delta\beta_1 = -7$ ps/m, shown in the central column. The lower probe group velocity moved the probe towards the trailing edge of the pump, so the same average temporal overlap as for $\Delta\beta_1 = 7$ ps/m resulted in significantly reduced XPM-assisted Raman amplification in the probe and a higher probe coherence of $\langle|g_{12}^{(1)}|\rangle = 0.6$.

It was possible to maintain a high probe coherence for a positive GVM only if the GVM was increased substantially. Using $\Delta\beta_1 = 10$ ps/m (third column, Fig. 5) maintained an average probe coherence of 0.6. For this GVM, the probe reached a delay approximating the pump FWHM duration after propagating $L_{c\,\mathrm{pump}} = 72$ cm, so temporal overlap of the pulses was small by the time that Raman scattering had become significant for the pump.

1. *Competition between Optical Wavebreaking and Raman-Assisted Parametric FWM*

The competition between optical wavebreaking and Raman-assisted parametric FWM determines whether the supercontinuum process in ANDi fiber is coherent or incoherent [9]. This competition is parameterized by the coherence length, L_c [Eq. (6)], at which $\langle|g_{12}^{(1)}|\rangle$ decreases to 0.9. Since L_{WB} increases if the pulse duration is increased, even if the peak power is held constant, this results in a reduced coherence length and a faster rate of decoherence. In this section, by adding XPM, we provide the first study of the probe coherence as the pump transitions from coherent to incoherent propagation dynamics.

We calculated the average coherence for both the pump and the probe over a broad range of GVM, pump energy, and duration values while maintaining a fixed pump peak power of 15 kW (approximating values commonly used in experiments and simulations [3,7,9]). We parameterize the pump characteristics using N_{pump} [Eq. (7)] and use a constant peak power to fix $L_N = 2.5$ mm ($\gamma P_0 = 405$ rad/m). The pump duration

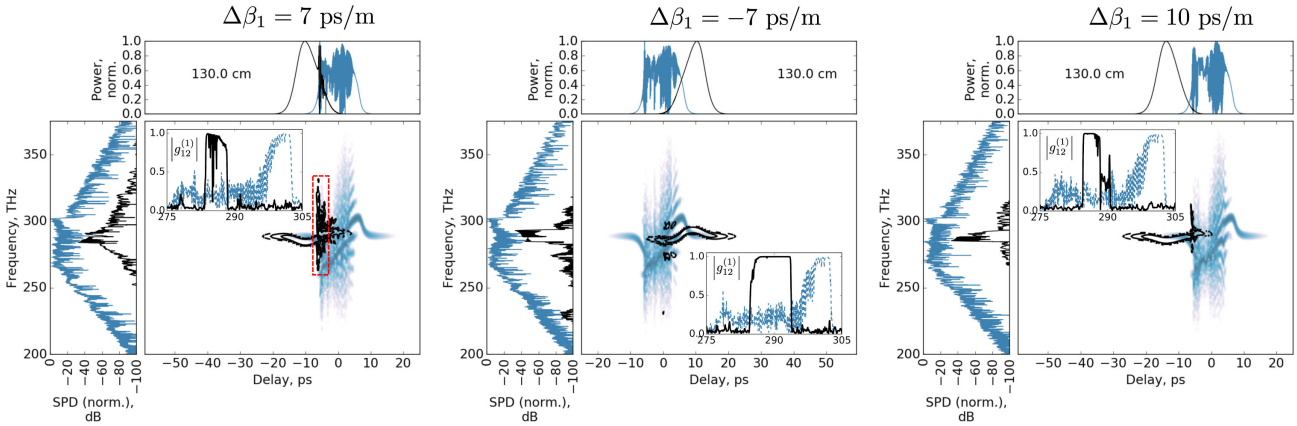

Fig. 5. Decoherence of orthogonally polarized pump and probe pulses with the same central wavelength (1040 nm, 288 THz), shown by the blue colormap and black contour, respectively, as a function of group velocity mismatch. Both the magnitude and sign of $\Delta\beta_1$ change the degradation of the probe coherence. $E_{\mathrm{pump}} = 60$ nJ, $E_{\mathrm{probe}} = 5$ pJ, $T_0 = 7$ ps, and $L_{\mathrm{fiber}} = 130$ cm. Columns from left to right: $\Delta\beta_1 = 7$ ps/m, −7 ps/m, and 10 ps/m. Insets: pump coherence (blue dashed) and probe coherence (solid black) as a function of frequency (THz) over the region of highest spectral power density.

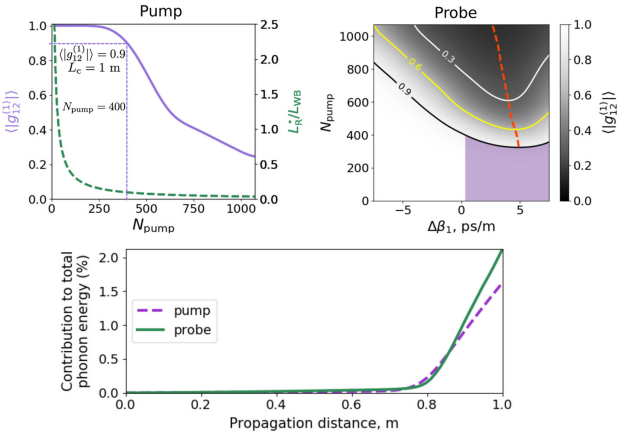

Fig. 6. Top left: Average pump coherence (left y axis, purple solid line) and $L_R^\star/L_{WB}$ (right y axis, green dashed line) as a function of N_{pump} for a 1 m length of PCF. Top right: average probe coherence as a function of N_{pump} and $\Delta\beta_1$ for a 1 m length of PCF. The red dashed line in the right-hand plot shows where $\langle|g_{12}^{(1)}|\rangle$ is minimized for a given N_{pump}. The purple region shows where $L_{c\,probe}$ is shorter than $L_{c\,pump}$, and therefore where the decoherence for the probe occurs at a higher rate than the pump. Bottom: energy transferred from the pump and probe pulses to the phonon field as a function of propagation distance ($N_{pump} = 900$ and $\Delta\beta_1 = 0$ ps/m).

ranged from 0.1 ps to 7 ps and the pump energy from 1.6 nJ to 112 nJ, giving $L_R^\star = 0.1$ m while varying L_{WB} from 0.04 m to 2.9 m to show the effect of both coherent and incoherent pump dynamics on the probe. The probe energy and duration were held constant at 5 pJ and 7 ps ($P_0 \approx 0.7$ W), giving probe nonlinear and dispersion lengths of 61 m and 2.7 km, respectively, ensuring that Eq. (1) was fulfilled for the full parameter space. The results are shown in Fig. 6. Due to the PCF length of 1 m, the $\langle|g_{12}^{(1)}|\rangle = 0.9$ contour in Fig. 6 gives the pairs of $\Delta\beta_1$ and N_{pump} values resulting in $L_{c\,probe} = 1$ m.

The average pump coherence (Fig. 6, top left) had no GVM dependence because Eq. (1) was fulfilled. For clarity, we therefore show the average pump coherence for $\Delta\beta_1 = 0$ ps/m only. $L_{c\,pump} = 1$ m for $N_{pump} = 400$ ($E_{pump} \approx 42$ nJ, $T_0 = 2.7$ ps), shown by the purple dashed lines. The variation of $L_{c\,pump} \propto L_R^\star/L_{WB}$ versus pump parameters and fiber dispersion is also shown. The transition from optical wavebreaking to Raman-assisted parametric FWM occurs for $N_{pump} \approx 400$.

Our previous observation that the probe coherence is reduced more quickly for $\Delta\beta_1 > 0$ ps/m is shown here by the asymmetry of the $\langle|g_{12}^{(1)}|\rangle$ contours around $\Delta\beta_1 = 0$ ps/m (Fig. 6, top right). The minimum N_{pump} that results in $L_{c\,probe} = 1$ m occurs at $\Delta\beta_1 = 5$ ps/m. For large $|\Delta\beta_1|$ values, $L_{c\,probe} = 1$ m is maintained only if the pump soliton order increases linearly with $|\Delta\beta_1|$.

The asymmetry of the probe decoherence with GVM becomes less significant as N_{pump} (and thus the pump decoherence rate) is increased. This is shown by the negative gradient of the red dashed line (Fig. 6, top right), which tracks the minimum probe coherence for each N_{pump}, and happens because Raman amplification occurs at the leading edge of the pump first and then progresses through the peak towards the trailing edge [9], and this progression occurs earlier in the propagation as N_{pump} is increased.

2. Accelerated Decoherence for Low-Energy Probe

Figure 6 shows that for some values of N_{pump} and $\Delta\beta_1$, the probe coherence degrades further than that of the pump despite the reduction in the pump influence on the probe by $\epsilon_{XPM} = 2/3$ [Eq. (A3)]. This is most pronounced when the probe energy is significantly smaller than the pump energy. For example, the average pump coherence is equal to 0.3 when $N_{pump} = 950$, but the average probe coherence takes the same value between $-2 \le \Delta\beta_1 \le 7$ ps/m and $630 \le N_{pump}$ (shown by the white contour), where $E_{probe} \approx 10^{-4} E_{pump}$. The region where the pump coherence exceeds the probe coherence is confined to smaller ranges of $\Delta\beta_1$ as N_{pump} is decreased, until eventually the pump coherence is higher only when the probe pulse propagates faster than the pump pulse. These effects can be understood by examining the mixed parametric-Raman gain for the first Stokes waves of the pump and probe [9,24–26], which take comparable values of $g_s^\star P_0 = 9.6\ \mathrm{m}^{-1}$ and $(2/3)g_s^\star P_0 = 6.4\ \mathrm{m}^{-1}$ for an average probe coherence of 0.3 at $\Delta\beta_1 = 0$ ps/m (where $N_{pump} \approx 800$, $T_0 = 5.3$ ps, and $E_{pump} = 85$ nJ). The low probe energy combined with the comparable Raman gain and equal Stokes seed energy (set by the quantum noise) results in a higher fraction of the probe energy being transferred to the Stokes and anti-Stokes waves:

$$\alpha_P(z) = \frac{E(z)}{E_{input}} - \alpha_{fiber}(z). \tag{8}$$

We attempted to calculate the energy in the pump and probe Stokes and anti-Stokes waves directly, but it is often not possible to separate the characteristics of each nonlinear process in the noisy spectra accurately. The total energy transferred to the phonon field (i.e., the energy loss due to the frequency detuning between the pulses and the Stokes waves) is an equivalent metric, obtained using Eq. (8). $E(z)/E_{input}$ gives the fractional energy loss for the pulses at propagation distance z, $\alpha_{fiber}(z)$ is the fractional energy loss from linear propagation in the fiber, and $\alpha_P(z)$ is the fractional energy lost by the pulses to the phonon field through Raman amplification. This quantity is reliable because of the negligible error introduced by our chosen integration method, because SPM, self-steepening, and dispersive pulse broadening are lossless, and because of the higher gain for the Stokes waves in comparison with the anti-Stokes waves [9,24–26], causing a net transfer of energy to the phonon field from the pump and probe pulses.

The contribution to the phonon energy from the pump and probe is shown as a percentage of their respective input energies in the bottom row of Fig. 6 for $N_{pump} = 900$ ($T_0 = 6$ ps, $E_{pump} \approx 95$ nJ) and $\Delta\beta_1 = 0$ ps/m. At the fiber output, the probe has contributed 2.2% of its energy to the phonon field for PCF lengths above 0.8 m, whereas the pump has contributed 1.6% in that section of the fiber, which confirms the proposed explanation for the relative coherences of the pump and probe. Equivalently, the average probe coherence is expected to be proportional to the probe energy as long as Eq. (1) is satisfied. This is confirmed by Fig. 7, which shows how $\langle|g_{12,probe}|\rangle$ depends on the ratio of probe energy to pump energy for a constant

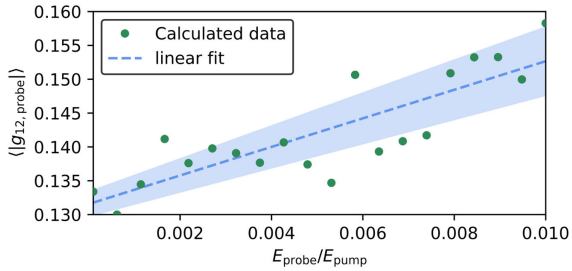

Fig. 7. Average probe coherence for 1 m of ANDi PCF with $\Delta\beta_1 = 0$ ps/m as a function of the ratio of the probe energy to the pump energy. The pulse durations were constant at 7 ps, and the pump energy was held constant at 60 nJ. The shaded region shows the confidence interval of the linear fit to one standard deviation.

pump energy of 60 nJ ($\Delta\beta_1 = 0$ ps/m, $T_{\mathrm{pump}} = 7$ ps giving $L_{\mathrm{N}} = 4.5$ mm, $L_{\mathrm{D}} = 2.75$ km, and $N_{\mathrm{pump}} = 780$). The fitted curve shows that the relationship has a dominant linear component, which is given by $(2.11 \pm 0.3)\,E_{\mathrm{probe}}/E_{\mathrm{pump}}$ for the pulse and fiber parameters chosen.

We note that the accelerated probe decoherence is important for a very broad range of GVM values, and occurs faster than the pump decoherence (top right plot in Fig. 6, purple shading) when $N_{\mathrm{pump}} > 300$ and when $\Delta\beta_1$ is between 0.3 and 8 ps/m. The corresponding birefringence of 9×10^{-5} to 2.4×10^{-3} covers both non-PM and PM fibers. The faster loss of coherence for low-energy signal propagating with an incoherently broadened high-energy pulse is therefore expected whenever it is polarized along the fiber fast (lower index) axis.

B. Co-Polarized, Cross-Wavelength Decoherence

Figure 8 shows co-polarized pump and probe pulses in the same format as Figs. 4 and 5 and for the same fiber parameters. The pump central wavelength was constant at 1040 nm, but the probe was set to 1100 nm (top row of Fig. 8), and 1300 nm (bottom row) to explore how the fiber dispersion affects the probe decoherence. The pulse duration was 7 ps (probe bandwidths of 0.25 nm and 0.35 nm, respectively, and a pump bandwidth of 0.23 nm). Differences in the propagation for co-polarized pulses in comparison with cross-polarized pulses are due to the increased strength of XPM, which is three times higher compared with the cross-polarized case.

The GVM was just 2 ps/m for a probe central wavelength of 1100 nm, so its large overlap with the pump leading edge caused significant Raman amplification. The Raman gain for the pump was $g_s^\star P_0 = 7\ \mathrm{m}^{-1}$ [$L_{\mathrm{R}}^\star = 14$ cm, $N_{\mathrm{pump}} = 770$; see Eqs. (2) and (3)], but the gain for the probe was higher at approximately $15.3\ \mathrm{m}^{-1}$ because $\epsilon_{\mathrm{XPM}} = 2$ for co-polarized pulses [Eq. (A3)] and because of the different dispersion values at the pump and probe wavelengths. The Raman gain for the 1300 nm probe (bottom row of Fig. 8) was $22.5\ \mathrm{m}^{-1}$, but the effect is reduced by the larger GVM of ~ 9 ps/m. The larger Raman gain means the probe coherence degraded faster than for the orthogonally polarized pump and probe in Section 3.A. In the top row of Fig. 8, the probe coherence degraded to $\langle|g_{12}^{(1)}|\rangle = 0.15$ compared to $\langle|g_{12}^{(1)}|\rangle = 0.24$ for the pump. $L_{\mathrm{c\,pump}} = 72$ cm, and

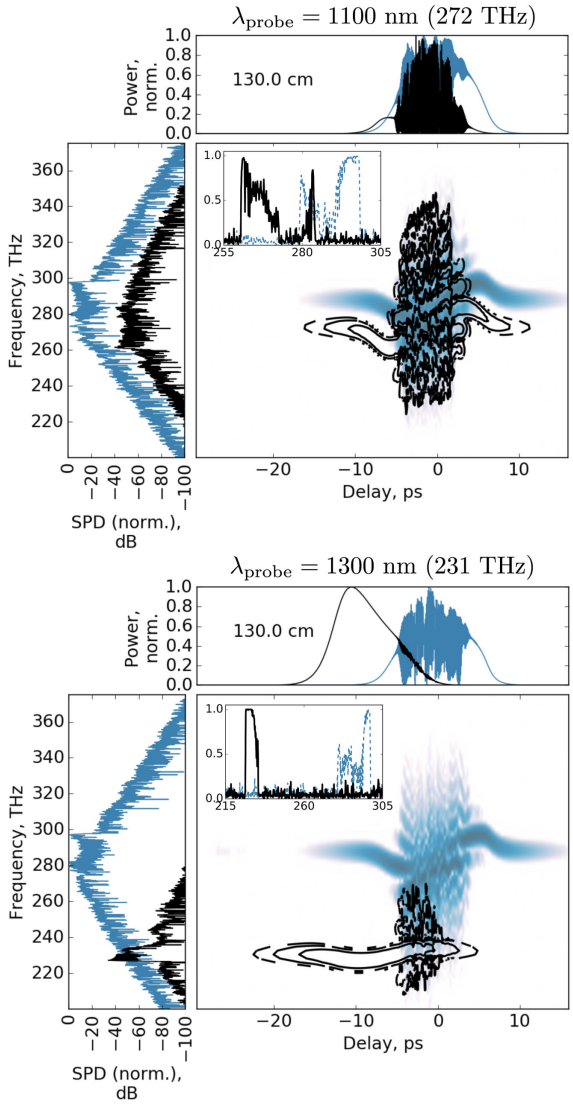

Fig. 8. Cross-wavelength decoherence for co-polarized pump and probe (XPM factor of 2). $T_0 = 7$ ps and $L_{\mathrm{fiber}} = 130$ cm for all simulations, and the pulses have zero initial relative delay. Top: $\lambda_{\mathrm{c\,pump}} = 1040$ nm (288 THz), $\lambda_{\mathrm{c\,probe}} = 1100$ nm (273 THz). Bottom: $\lambda_{\mathrm{c\,pump}} = 1040$ nm, $\lambda_{\mathrm{c\,probe}} = 1300$ nm (231 THz). Insets: pump and probe coherence for the region of highest spectral power density (dashed blue and solid black lines, respectively).

$L_{\mathrm{c\,probe}}$ was 71 cm and 83 cm for the two wavelengths, respectively (compare with equivalent average coherence values for cross-polarized probe pulses, where $N_{\mathrm{pump}} = 770$ and $\Delta\beta_1 = 2$ and 9 ps/m: 0.23 and 0.57, respectively). The fiber dispersion profile therefore has a similar influence on the probe coherence to the polarization GVM, except the probe Raman gain is higher because of the stronger influence of XPM.

For completeness, note that the most general case of XPM-assisted decoherence occurs for cross-polarized pulses with different central wavelengths. For those conditions, the probe decoherence will be a function of the pulse polarization state as well as the fiber polarization GVM and dispersion. Although the size of this parameter space goes beyond the scope of the current work, the two cases outlined in Sections 3.A and 3.B

provide insights that are useful for predicting the propagation dynamics in the more general case. For example, cross-polarized pump and probe pulses with respective central wavelengths of 1040 nm and 900 nm would have a GVM of −6.2 ps/m for the PCF used in this work, and so, in a weakly birefringent fiber, the probe would develop in a way similar to the $\Delta\beta_1 = -7$ ps/m simulation in Fig. 5. However, were the probe propagated with its polarization aligned to the fast (low-index) axis of a highly birefringent fiber instead, then this GVM would be counteracted, resulting in a more significant loss of coherence for the probe. Note that we have chosen wavelength offsets that are mismatched from the Raman gain peak at 13.2 THz to avoid coherently seeded Raman amplification.

4. CONCLUSION

We have studied a new mechanism through which the ANDi supercontinuum decoherence process can be transferred to a co-propagating probe signal via a combination of XPM and Raman amplification of out-of-band quantum noise. We have systematically characterized the mechanism using a vector GNLSE to investigate the decoherence of a low-energy probe that co-propagates with a high-energy, continuum-generating pump. Our work extends a scalar investigation that showed that Raman decoherence is highly significant for picosecond pulses in meter-length fibers [9] to include XPM-based nonlinear coupling.

We explored a broad range of pulse and fiber parameters such as fiber birefringence, pulse durations, peak powers, central wavelengths, and the assignment of the pump and probe pulses to both the fast and slow polarization axes. The pump pulses investigated had sufficient energy and duration to undergo substantial decoherence over fiber lengths of approximately 1 m if propagated on their own. For the probe, we chose pulse parameters that resulted in a negligible contribution to nonlinear and dispersive effects.

The main conclusion is that there is an asymmetry in the probe decoherence versus the sign of the GVM. This effect can be observed only using vector simulations, and occurs because the temporal overlap of the probe pulse with the Raman amplification in the pump leading edge is maximized when the probe has a higher group velocity. This is the case when an orthogonally polarized probe is propagated along the fast (lower index) axis of the fiber, or when a co-polarized probe has a longer central wavelength, and occurs in both PM and non-PM fibers. The polarization GVM and the fiber dispersion have equivalent roles in the probe decoherence for narrow-band input pulses, and so the PCF hole and pitch size as well as the birefringence will determine the probe coherence in general. The relative polarization state of the pump and probe was also found to be of central importance as it determines the strength of the XPM coupling between the pulses. We also observed that the probe decoherence can occur at a higher rate where the probe energy is sufficiently small, and that this happens for both orthogonally and co-polarized probes.

APPENDIX A. GENERALIZED NONLINEAR SCHRÖDINGER EQUATION

We simulated the nonlinear propagation of both the pump and probe using Eq. (A1). Operators $\hat{D}$ and $\hat{N}$ are responsible for linear and nonlinear effects acting on field envelope $A(z, T)$:

$$\frac{\partial A(z, T)}{\partial z} = \left(\hat{D} + \hat{N}\right) A(z, T). \tag{A1}$$

We took the standard approach of applying the fiber dispersion and loss in the frequency domain using the linear operator defined in Eq. (A2):

$$\hat{D}(\Omega) = \frac{\alpha(\Omega)}{2} - i\left[\Delta\beta_1\Omega - \frac{\beta_2(\Omega)}{2}\Omega^2\right], \tag{A2}$$

where $\alpha(\Omega)$ is the fiber loss spectrum, $\beta_2(\Omega)$ is the full fiber group velocity dispersion (its frequency dependence accounts for the higher orders), and $\Omega = \omega - \omega_0$ is the angular frequency grid centered on zero. The polarization GVM is accounted for using $\Delta\beta_1$ as described in Section 2 and, being the difference between the pump and probe group velocities, was included for orthogonally polarized probe pulses only to keep the pump pulse centered at the origin of the temporal grid. The fiber dispersion determined the GVM for co-polarized pulses.

Although the nonlinear operator is commonly defined in the time domain, we opted for the frequency domain definition given by Eq. (A3) to account for the frequency dependence of γ and because this definition is more readily incorporated into the CQEM [42]:

$$\hat{N}_{\text{pump}}(\Omega) = -i\gamma(\Omega)\left(1 + \frac{\Omega}{\omega_0}\right)\left(\mathcal{F}[(1 - f_R)(|A_{\text{pump}}(z, T)|^2 + \epsilon_{\text{XPM}}|A_{\text{probe}}(z, T)|^2)\right.$$
$$\left. + f_R\mathcal{F}^{-1}[\tilde{h}_R(\Omega)\mathcal{F}[|A_{\text{pump}}(z, T)|^2 + |A_{\text{probe}}(z, T)|^2]] + i\Gamma_R(z, T)]\right). \tag{A3}$$

For the probe propagation, $\hat{N}_{\text{probe}}$ takes the same form as Eq. (A3), but $A_{\text{pump}}(z, T)$ and $A_{\text{probe}}(z, T)$ are swapped. $\mathcal{F}$ and $\mathcal{F}^{-1}$ denote the fast Fourier transform and its inverse, respectively. XPM is included using $\epsilon_{\text{XPM}}|A(z, T)|^2$, where $\epsilon_{\text{XPM}} = 2/3$ or 2 for orthogonally polarized or co-polarized pulses, respectively. $\tilde{h}_R(\Omega)$ is the Raman response of the fiber, and $\Gamma_R(z, T)$ accounts for spontaneous Raman scattering noise [10,48]. We neglected the degenerate FWM term given by $A^{\star}_{\text{pump}}A^2_{\text{probe}}\exp(-4i\Delta nz/\lambda)$ (or, for the probe $A^{\star}_{\text{probe}}A^2_{\text{pump}}\exp(4i\Delta nz/\lambda)$) because we found that its contribution averaged to zero [46], where $\Delta n > 3 \times 10^{-5}$ (corresponding to $|\Delta\beta_1| > 0.1$ ps/m, which covers the majority of the GVM range explored), and also because our aim was to

investigate the effects of XPM-assisted Raman amplification on the probe decoherence in isolation from other field coupling effects. Additionally, a Raman term involving the product of both A_1 and A_2 had a negligible effect for the pump and probe energies selected, and so was excluded to reduce computation time.

Funding. Engineering and Physical Sciences Research Council (EP/P012248/1, EP/P027644/1, EP/P030181/1); U.S. Air Force Office of Scientific Research (FA9550-14-1-0382).

Acknowledgment. J. S. Feehan acknowledges SCAPA (University of Strathclyde) for support. Data from the figures are available from the University of Strathclyde repository at Ref. [53].

Disclosures. The authors declare no conflicts of interest.

REFERENCES

1. P. Falk, M. H. Frosz, and O. Bang, "Supercontinuum generation in a photonic crystal fiber with two zero-dispersion wavelengths tapered to normal dispersion at all wavelengths," Opt. Express **13**, 7535–7540 (2005).
2. L. E. Hooper, P. J. Mosley, A. C. Muir, W. J. Wadsworth, and J. C. Knight, "Coherent supercontinuum generation in photonic crystal fiber with all-normal group velocity dispersion," Opt. Express **19**, 4902–4907 (2011).
3. A. M. Heidt, A. Hartung, G. W. Bosman, P. Krok, E. G. Rohwer, H. Schwoerer, and H. Bartelt, "Coherent octave spanning near-infrared and visible supercontinuum generation in all-normal dispersion photonic crystal fibers," Opt. Express **19**, 3775–3787 (2011).
4. W. J. Tomlinson, R. H. Stolen, and A. M. Johnson, "Optical wave breaking of pulses in nonlinear optical fibers," Opt. Lett. **10**, 457–459 (1985).
5. D. Anderson, M. Desaix, M. Lisak, and M. L. Quiroga-Teixeiro, "Wave breaking in nonlinear-optical fibers," J. Opt. Soc. Am. B **9**, 1358–1361 (1992).
6. C. Finot, B. Kibler, L. Provost, and S. Wabnitz, "Beneficial impact of wave-breaking for coherent continuum formation in normally dispersive nonlinear fibers," J. Opt. Soc. Am. B **25**, 1938–1948 (2008).
7. A. M. Heidt, "Pulse preserving flat-top supercontinuum generation in all-normal dispersion photonic crystal fibers," J. Opt. Soc. Am. B **27**, 550–559 (2010).
8. A. M. Heidt, J. Rothhardt, A. Hartung, H. Bartelt, E. G. Rohwer, J. Limpert, and A. Tünnermann, "High quality sub-two cycle pulses from compression of supercontinuum generated in all-normal dispersion photonic crystal fiber," Opt. Express **19**, 13873–13879 (2011).
9. A. M. Heidt, J. S. Feehan, J. H. V. Price, and T. Feurer, "Limits of coherent supercontinuum generation in normal dispersion fibers," J. Opt. Soc. Am. B **34**, 764–775 (2017).
10. J. M. Dudley, G. Genty, and S. Coen, "Supercontinuum generation in photonic crystal fiber," Rev. Mod. Phys. **78**, 1135–1184 (2006).
11. N. Nishizawa, Y. Chen, P. Hsiung, E. P. Ippen, and J. G. Fujimoto, "Real-time, ultrahigh-resolution, optical coherence tomography with an all-fiber, femtosecond fiber laser continuum at 1.5μm," Opt. Lett. **29**, 2846–2848 (2004).
12. G. Humbert, W. J. Wadsworth, S. G. Leon-Saval, J. C. Knight, T. A. Birks, P. S. J. Russell, M. J. Lederer, D. Kopf, K. Wiesauer, E. I. Breuer, and D. Stifter, "Supercontinuum generation system for optical coherence tomography based on tapered photonic crystal fibre," Opt. Express **14**, 1596–1603 (2006).
13. T. Udem, R. Holzwarth, and T. W. Hänsch, "Optical frequency metrology," Nature **416**, 233–237 (2002).
14. R. Holzwarth, T. Udem, T. W. Hänsch, J. C. Knight, W. J. Wadsworth, and P. S. J. Russell, "Optical frequency synthesizer for precision spectroscopy," Phys. Rev. Lett. **85**, 2264–2267 (2000).
15. C. R. Head, H. Y. Chan, J. S. Feehan, D. P. Shepherd, S. Alam, A. C. Tropper, J. H. V. Price, and K. G. Wilcox, "Supercontinuum generation with GHz repetition rate femtosecond-pulse fiber-amplified VECSELs," IEEE Photon. Technol. Lett. **25**, 464–467 (2013).
16. J. H. V. Price, X. Feng, A. M. Heidt, G. Brambilla, P. Horak, F. Poletti, G. Ponzo, P. Petropoulos, M. Petrovich, J. Shi, M. Ibsen, W. H. Loh, H. N. Rutt, and D. J. Richardson, "Supercontinuum generation in non-silica fibers," Opt. Fiber Technol. **18**, 327–344 (2012).
17. S. Xing, S. Kharitonov, J. Hu, and C.-S. Brès, "Linearly chirped mid-infrared supercontinuum in all-normal-dispersion chalcogenide photonic crystal fibers," Opt. Express **26**, 19627–19636 (2018).
18. M. Klimczak, B. Siwicki, A. Heidt, and R. Buczyński, "Coherent supercontinuum generation in soft glass photonic crystal fibers," Photon. Res. **5**, 710–727 (2017).
19. M. Diouf, A. B. Salem, R. Cherif, H. Saghaei, and A. Wague, "Superflat coherent supercontinuum source in $As_{38.8}Se_{61.2}$ chalcogenide photonic crystal fiber with all-normal dispersion engineering at a very low input energy," Appl. Opt. **56**, 163–169 (2017).
20. H. Timmers, A. Kowligy, A. Lind, F. C. Cruz, N. Nader, M. Silfies, G. Ycas, T. K. Allison, P. G. Schunemann, S. B. Papp, and S. A. Diddams, "Molecular fingerprinting with bright, broadband infrared frequency combs," Optica **5**, 727–732 (2018).
21. L. Shen, N. Healy, P. Mehta, T. D. Day, J. R. Sparks, J. V. Badding, and A. C. Peacock, "Nonlinear transmission properties of hydrogenated amorphous silicon core fibers towards the mid-infrared regime," Opt. Express **21**, 13075–13083 (2013).
22. F. M. Mitschke and L. F. Mollenauer, "Discovery of the soliton self-frequency shift," Opt. Lett. **11**, 659–661 (1986).
23. J. P. Gordon, "Theory of the soliton self-frequency shift," Opt. Lett. **11**, 662–664 (1986).
24. E. A. Golovchenko, P. V. Mamyshev, A. N. Pilipetskii, and E. M. Dianov, "Mutual influence of the parametric effects and stimulated Raman scattering in optical fibers," IEEE J. Quantum Electron. **26**, 1815–1820 (1990).
25. S. Trillo and S. Wabnitz, "Parametric and Raman amplification in birefringent fibers," J. Opt. Soc. Am. B **9**, 1061–1082 (1992).
26. S. Coen, D. A. Wardle, and J. D. Harvey, "Observation of non-phase-matched parametric amplification in resonant nonlinear optics," Phys. Rev. Lett. **89**, 273901 (2002).
27. I. B. Gonzalo and O. Bang, "Role of the Raman gain in the noise dynamics of all-normal dispersion silica fiber supercontinuum generation," J. Opt. Soc. Am. B **35**, 2102–2110 (2018).
28. I. B. Gonzalo, R. D. Engelsholm, M. P. Sørensen, and O. Bang, "Polarization noise places severe constraints on coherence of all-normal dispersion femtosecond supercontinuum generation," Sci. Rep. **8**, 6579 (2018).
29. E. Genier, P. Bowen, T. Sylvestre, J. M. Dudley, P. Moselund, and O. Bang, "Amplitude noise and coherence degradation of femtosecond supercontinuum generation in all-normal-dispersion fibers," J. Opt. Soc. Am. B **36**, A161–A167 (2019).
30. J. E. Sharping, M. Fiorentino, P. Kumar, and R. S. Windeler, "All-optical switching based on cross-phase modulation in microstructure fiber," IEEE Photon. Technol. Lett. **14**, 77–79 (2002).
31. B.-E. Olsson and D. J. Blumenthal, "All-optical demultiplexing using fiber cross-phase modulation (XPM) and optical filtering," IEEE Photon. Technol. Lett. **13**, 875–877 (2001).
32. M. E. Fermann, M. J. Andrejco, Y. Silberberg, and M. L. Stock, "Passive mode locking by using nonlinear polarization evolution in a polarization-maintaining erbium-doped fiber," Opt. Lett. **18**, 894–896 (1993).
33. K. Tamura, E. P. Ippen, H. A. Haus, and L. E. Nelson, "77-fs pulse generation from a stretched-pulse mode-locked all-fiber ring laser," Opt. Lett. **18**, 1080–1082 (1993).
34. G. P. Agrawal, "Modulation instability induced by cross-phase modulation," Phys. Rev. Lett. **59**, 880–883 (1987).
35. G. P. Agrawal, P. L. Baldeck, and R. R. Alfano, "Modulation instability induced by cross-phase modulation in optical fibers," Phys. Rev. A **39**, 3406–3413 (1989).

36. D. Dobrakowski, A. Rampur, G. Stępniewski, A. Anuszkiewicz, J. Lisowska, D. Pysz, R. Kasztelanic, and M. Klimczak, "Development of highly nonlinear polarization-maintaining fibers with normal dispersion across entire transmission window," J. Opt. **21**, 015504 (2018).
37. K. Tarnowski, T. Martynkien, P. Mergo, K. Poturaj, A. Anuszkiewicz, P. Béjot, F. Billard, O. Faucher, B. Kibler, and W. Urbanczyk, "Polarized all-normal dispersion supercontinuum reaching 2.5 μm generated in a birefringent microstructured silica fiber," Opt. Express **25**, 27452–27463 (2017).
38. R. G. Smith, "Optical power handling capacity of low loss optical fibers as determined by stimulated Raman and Brillouin scattering," Appl. Opt. **11**, 2489–2494 (1972).
39. R. H. Stolen, J. P. Gordon, W. J. Tomlinson, and H. A. Haus, "Raman response function of silica-core fibers," J. Opt. Soc. Am. B **6**, 1159–1166 (1989).
40. J. Hult, "A fourth-order Runge-Kutta in the interaction picture method for simulating supercontinuum generation in optical fibers," J. Lightwave Technol. **25**, 3770–3775 (2007).
41. A. M. Heidt, "Efficient adaptive step size method for the simulation of supercontinuum generation in optical fibers," J. Lightwave Technol. **27**, 3984–3991 (2009).
42. A. A. Rieznik, A. M. Heidt, P. G. Konig, V. A. Bettachini, and D. F. Grosz, "Optimum integration procedures for supercontinuum simulation," IEEE Photon. J. **4**, 552–560 (2012).
43. M. Koshiba and K. Saitoh, "Applicability of classical optical fiber theories to holey fibers," Opt. Lett. **29**, 1739–1741 (2004).
44. K. Saitoh and M. Koshiba, "Empirical relations for simple design of photonic crystal fibers," Opt. Express **13**, 267–274 (2005).
45. T. Miya, Y. Terunuma, T. Hosaka, and T. Miyashita, "Ultimate low-loss single-mode fibre at 1.55μm," Electron. Lett. **15**, 106–108 (1979).
46. G. P. Agrawal, *Nonlinear Fiber Optics*, 4th ed. (Academic, 2006).
47. J. S. Feehan, F. Ö. Ilday, W. S. Brocklesby, and J. H. V. Price, "Simulations and experiments showing the origin of multiwavelength mode locking in femtosecond, Yb-fiber lasers," J. Opt. Soc. Am. B **33**, 1668–1676 (2016).
48. P. D. Drummond and J. F. Corney, "Quantum noise in optical fibers. I. Stochastic equations," J. Opt. Soc. Am. B **18**, 139–152 (2001).
49. M. H. Frosz, "Validation of input-noise model for simulations of supercontinuum generation and rogue waves," Opt. Express **18**, 14778–14787 (2010).
50. N. R. Newbury and W. C. Swann, "Low-noise fiber-laser frequency combs (Invited)," J. Opt. Soc. Am. B **24**, 1756–1770 (2007).
51. J. M. Dudley and S. Coen, "Coherence properties of supercontinuum spectra generated in photonic crystal and tapered optical fibers," Opt. Lett. **27**, 1180–1182 (2002).
52. J. M. Dudley and S. Coen, "Numerical simulations and coherence properties of supercontinuum generation in photonic crystal and tapered optical fibers," IEEE J. Sel. Top. Quantum Electron **8**, 651–659 (2002).
53. https://www.doi.org/10.15129/a254c0da-7324-4215-8430-ad383122de12.